Slip Distribution of the 2017 M_w6.6 Bodrum-Kos Earthquake: Resolving the Ambiguity of Fault Geometry

A. Ozgun Konca[(1)], Sezim Ezgi Guvercin[(1)], Seda Ozarpaci[(2)], Alpay Ozdemir[(2)], Gareth J. Funning[(3)] , Ugur Dogan[(2)], Semih Ergintav[(4)], Michael Floyd[(5)], Hayrullah Karabulut[(1)], and Robert Reilinger[(5)],

(1) Bogazici University, Kandilli Observatory and Earthquake Research Institute, Dept of Geophysics, Istanbul, Turkey (ozgun.konca@boun.edu.tr)

(2) Yildiz Technical University, Dept of Geomatic, Istanbul, Turkey

(3) UC Riverside, Department of Earth Sciences, Riverside, CA, USA

(4) Bogazici University, Kandilli Observatory and Earthquake Research Institute, Dept. of Geodesy, Istanbul, Turkey

(5) Massachusetts Institute of Technology, Dept of Earth, Atmospheric and Planetary Sciences, Cambridge, MA, USA

Summary

The 20 July 2017, M_w6.6 Bodrum-Kos Earthquake occurred in the Gulf of Gökova in the SE Aegean, a region characterized by N-S extension in the back-arc of the easternmost Hellenic Trench. The dip direction of the fault that ruptured during the earthquake has been a matter of controversy where both north and south-dipping fault planes were used to model the coseismic slip in previous studies. Here, we use seismic (seismicity, mainshock modeling, aftershock relocations and aftershock mechanisms using regional body and surface waves), geodetic (GPS, InSAR), and structural observations to estimate the location, and the dip direction of the fault that ruptured during the 2017 earthquake, and the relationship of this event to regional tectonics. We consider both dip directions and systematically search for the best-fitting locations for the north- and south-dipping fault planes. Comparing the best-fitting planes for both dip directions in terms of their misfit to the geodetic data, proximity to the hypocenter location and Coulomb stress changes at the aftershock locations, we conclude that the 2017 earthquake ruptured a north-dipping fault. We find that the

earthquake occurred on a 20-25 km long, ~E-W striking, 40° north-dipping, pure normal fault with slip primarily confined between 3-15 km depth, and the largest slip exceeding 2 m between depths of 4-10 km. The coseismic fault, not mapped previously, projects to the surface within the western Gulf, and partly serves both to widen the Gulf and separate Kos Island from the Bodrum Peninsula of SW Anatolia. The coseismic fault may be an extension of a mapped, north-dipping normal fault along the south side of the Gulf of Gökova. While all of the larger aftershocks are consistent with N-S extension, their spatially dispersed pattern attests to the high degree of crustal fracturing within the basin, due to rapid trench-ward extension and anticlockwise rotation within the southeastern Aegean.

Keywords: Earthquake source observations Satellite Geodesy Seismicity and tectonics Europe

Introduction

On 20 June 2017, an M_w6.6 earthquake struck between the Bodrum Peninsula of southeast Turkey and Kos Island, Greece, in the easternmost Aegean Sea (Figure 1). The earthquake caused the deaths of two people and injured hundreds, and produced significant structural damage in Bodrum and Kos Island. In addition, the earthquake induced a local tsunami with wave heights reaching 1.4 m (Heidarzadeh *et al.*, 2017; Yalçıner *et al.*, 2017). Source mechanisms show that the earthquake ruptured an E-W trending normal fault (Table 1), which is consistent with the general N-S extension in the SE Aegean region that is responsible for the opening of the Gulf of Gökova (Figure 1, see also McClusky *et al.*, 2000 Figure 7).

The initial finite-fault models of the earthquake based on GPS coseismic offsets assumed that the earthquake ruptured a south-dipping normal fault based in part on reported uplift along the Bodrum coast (Saltogianni *et al.*, 2017; Tiryakioğlu *et al.*, 2017). Other studies of the 2017 earthquake that included both GPS and InSAR observations showed significant negative displacement in the line of sight (LOS) direction from InSAR data on a small island called Karaada south of the Bodrum coastline,

that can be explained by a 40°, north-dipping fault plane (Ganas *et al.*, 2017). Later studies by Karasözen et al. (2018) and Ganas *et al.* (2019), based on horizontal GPS and InSAR data as well as aftershock distribution, also reported that the rupture occurred on a north-dipping fault.

This ambiguity of fault dip direction arises from two complicating factors. First, normal fault earthquakes can generate quite symmetric patterns of surface displacement in both horizontal and vertical directions, especially when the fault dip angle is close to 45° and the rupture does not reach the surface. Figure S1 shows a synthetic example, where slip is imposed on a 40° dipping normal fault (See Figure S1 caption for the details of the synthetic example). The resulting static displacements show that horizontal displacements are quite similar on either side of the fault. There is uplift both on the footwall side and on the hanging wall side beyond the hinge line. A second factor that contributes to the debate is that the aftershocks of the 2017 earthquake do not clearly show a preferred dip direction. They are distributed over a wide zone that makes it harder to differentiate the fault plane from the auxiliary plane.

The structural evidence whether south-dipping or the north-dipping faults are the main cause of the extension around the 2017 earthquake area is also debated. Kurt *et al.* (1999), investigated the shallow structure of Gulf of Gökova using multichannel seismic data. The reflection profiles along eastern gulf show that there are multiple horst and graben structures. On the other hand, in the western part of the gulf, where the 2017 earthquake struck, there are several south-dipping faults with surface expressions toward the north of the Gulf and one major north-dipping fault with significant vertical offset, named the Datça fault by the authors (Figure 2). A more recent study of the Gulf of Gökova based on multichannel seismic reflection (Ocakoğlu *et al.*, 2018) argued that the south-dipping faults with surface expressions on the northern edge of the Gulf are dominant, while the faults with surface expressions in the south are mostly oblique, left-lateral faults. On this basis, the authors suggest that the 2017 earthquake possibly broke a south-dipping fault.

Given various conflicting interpretations of the dip direction of the 2017 earthquake fault, we explore models for coseismic fault geometry and slip distribution for both north- and south-dipping faults. In order to find the best-fitting north- and south-dipping fault planes, we perform a grid search, where finite-fault models are generated centered at every grid point for both possible fault planes, using ascending and descending orbit InSAR data, and GPS estimates of horizontal and vertical coseismic displacements. We show that adding the vertical GPS displacements to the horizontal GPS and InSAR data provides sufficient constraints to differentiate between the two possible fault planes. Next, we compare the location of the hypocenter and aftershock locations with respect to the fault plane. We also determined the mechanism of the larger aftershocks following the mainshock, and compare the stress perturbations of the best-fitting north- and south-dipping fault planes to aftershock locations. The results of our study strongly support a north-dipping coseismic fault for the 2017 Bodrum-Kos earthquake.

Tectonic Setting

The Gulf of Gökova, where the 2017 Earthquake was located, is an ~E-W striking, extensional graben lying in the back-arc of the Hellenic subduction zone where it "abuts" southwest Anatolia (Figure 1). The Gulf is part of the Western Anatolia Extension Province that extends from the eastern Hellenic Trench north at least as far as the Izmir Peninsula and the Gediz and Buyuk Menderes Graben systems (e.g., Sengor *et al.*, 1984). The present-day rate of N-S extension across this region is about 20 mm/yr (McClusky *et al.*, 2000; Aktug *et al.*, 2009; Floyd *et al.*, 2010), with ~ 4 mm/yr across the Gulf of Gökova proper (Figure 1), or 20% of the total rate of extension. This high degree of extension is responsible for the large number of M>5 historic earthquakes that have occurred in the Gulf.

Structural studies indicate two phases of deformation in the Gulf region: During the Late Miocene, a phase of N-S compression and E-W extension, and the more recent Pliocene N-S extension that formed the present-day morphology of the Gulf, (e.g., Görür *et al.*, 1995; Gurer *et al.*, 2009). We note

that a Pliocene initiation of N-S extension is consistent with the present-day rate of extension across the Gulf (~4 mm/yr, Figure 1), and width of the Gulf (~20 km), providing an age estimate of ~ 5 Ma.

The underlying causes for these 2-phases of deformation are debated, but it is generally agreed that the initial compressive phase was associated with collision of the Hellenic-Cyprus arc system with Anatolia, followed in the Pliocene by N-S extension and anticlockwise rotation induced by retreat of the Hellenic Trench (e.g., Sengor *et al.*, 1984; Royden and Papanikolaou, 2011). The rotation of Late Miocene faults and dissection by younger, and presently active, E-W normal faults results in the complex system of faults that accommodate extension across the Gulf. The broadly distributed aftershock distribution of the 2017 earthquake (Figure 2) is consistent with this high degree of faulting.

Present-day morphology of the Gulf results from faulting on a set of normal fault segments (Figure 2) with the most prominent being the south-dipping, North Datça Fault system lying along the northern side of the Gulf, and the north-dipping, South Datça Fault system along the southern shoreline (Görür *et al.*, 1995; Emre *et al.*, 2013). On a more detailed scale, Kurt *et al.* (1999), investigated the shallow structure of the Gulf using multichannel seismic data. The reflection profiles along the eastern Gulf show multiple horst and graben structures aligned more or less east-west (Figure 2). In the western Gulf, where the 2017 earthquake struck, there are several south-dipping faults on the north side (Ocakoğlu *et al.,* 2018), and the north-dipping Datça Fault in the southern Gulf. Given the absence of an observed surface break, and the complexity and limited available information on faulting in the Gulf, the structural evidence for constraining the location and source of the 2017 coseismic fault is at best equivocal.

(e.g., Sengor *et al.*, 1984) (e.g., Sengor *et al.*, 1984; Royden and Papanikolaou, 2011)**Data and**

Methods

GPS Data

In this study, 12 continuous stations and 5 campaign GPS sites were used for the modeling of coseismic slip distribution. While many of the survey sites and continuous GPS stations (Table S1A and S1B, respectively) were present in the area before the Bodrum-Kos earthquake, most of them are on the Bodrum Peninsula (Figure 1). Five continuous GPS stations (TRKB, MUMC, ORTA, TGRT, YALI) are compiled from the network of the Association of Bodrum Geomatic Engineers (BODRUM-CORS), three stations (DATC, DIDI, and MUG1) are part of the Continuously Operating Reference Stations, Turkey (CORS-TR) and four stations (086A, 087A, KALY, RODO) from NOANET in Greece (Figure 1). Daily time series of 11 continuous GPS stations are shown in Figure S2.

In addition to the continuous data, we added 5 campaign sites to the analysis. The observations before the earthquake for the campaign sites were purchased from the General Directorate of Mapping, and the campaign sites were measured after the earthquake as part of this study.

The precise coordinates of the stations and secular velocity estimates were determined using GAMIT/GLOBK (10.6) software (Herring, 1998; Herring *et al.*, 2015). To estimate the coseismic displacements of campaign sites, we used a simple, linear model for the elastic strain accumulation to extrapolate the site position to the time immediately preceding the shock. We used the velocity field from Reilinger *et al.* (2006) to identify the pre-earthquake secular motions of campaign sites. Similarly, we used the same strategy to extrapolate positions measured after the earthquake back to the time immediately after the mainshock. The resulting coseismic displacements from survey sites are listed in Table S1A.

For the continuous stations, we used two days of observations before and after the earthquake (except MUMC) to estimate the coseismic displacements directly. MUMC had a problem before the

earthquake (9th of February 2017) and was re-activated after the earthquake (27th of July). The pre-earthquake position of MUMC was extrapolated from the station time series. The coseismic displacements for continuous GPS sites are tabulated in Table S1B.

InSAR data

The epicentral region of the Bodrum-Kos earthquake is covered by both ascending and descending tracks of the Copernicus/ESA Sentinel-1 satellite mission (Figure S3), and multiple acquisitions were made in the days and weeks following the event. We processed a selection of coseismic pairs of SAR images from both tracks into interferograms using the JPL/NASA ISCE software (Rosen *et al.*, 2011; Gurolla *et al.*, 2016), with a 30 m-resolution deformation model from the Shuttle Radar Topography Mission (Farr *et al.*, 2007) used to mitigate topographic artifacts. Selecting for the lowest levels of tropospheric noise present in each interferogram, assessed by visual inspection, we choose one ascending pair and one descending pair for further analysis (Table 2). We unwrap these interferograms using the SNAPHU algorithm (Chen and Zebker, 2002), and manually fix any unwrapping errors by isolating areas with anomalous phase (i.e. that do not match the phase of adjacent areas) and shifting them by multiples of 2π.

The original interferograms and the unwrapped range changes are shown for both tracks in Figure S3. The interferograms both have a high level of interferometric correlation on land and in the area surrounding the epicenter. The largest deformation gradients are located on the island of Karaada (Figure 2, Figure S3a), approximately 5 km south of Bodrum; both interferograms show positive range change of ~15-20 cm with respect to the Turkish mainland at the southern tip of Karaada, indicating that it subsided coseismically. To prepare the data for modeling, we applied a curvature-based quadtree decomposition (e.g. Simons *et al.*, 2002) focusing data sampling on features of interest in the data and reducing the number of data points in each interferogram from ~9 million to ~300.

Aftershock Relocation

We relocated the mainshock and aftershocks during the first 20 days following the mainshock using the catalogs of the General Directorate of Disaster Affairs of Turkey (AFAD), and Bogazici University Kandilli Observatory (KOERI) Regional Earthquake-Tsunami Monitoring Center (BDTIM) (see Figure S4 for the station distribution map). For the earthquakes that exist in both catalogs (AFAD and BDTIM), phase readings were merged. The earthquakes that existed only in one of the catalogs were also included in the joint catalog.

We revised the phase pickings using the continuous waveforms for the first 10 days (~1500 events) and used the phase pickings from the catalogs for the later days. The final presented catalog contains 2900 events between July 20 and August 7, 2017. The epicentral distribution is shown in Figure 2 and in Figure S5 for various time windows.

We relocated the earthquakes using the HYP program which is part of SEISAN Earthquake Analysis Software (Ottemöller *et al.*, 2013) that is based on Lienert *et al.* (1986). A 1-D velocity model was computed using the VELEST inversion code which minimizes travel time errors (Kissling *et al.*, 1994) (Table 3). The obtained P wave model is similar to the one obtained by Akyol *et al.* (2006) for southwest Turkey from earthquake relocations. The deviations from the 1-D velocity model are accounted for in the station corrections. Average location uncertainties are shown in Figure S6. The mean horizontal uncertainties are ~1.0 and ~1.8 km for latitude and longitude, respectively (Figure S6 a–b). The mean of the depth uncertainty is ~3 km with most events within the 2 and 4 km range (Figure S6c). The magnitude completeness threshold of the catalog is estimated as ~2.0 and the b-value is 1.1 (Figure Sd).

Aftershock Mechanisms

The mechanisms of aftershocks were studied using a subset from 83 broad-band stations of Kandilli Observatory and Research Institute (KOERI), General Directorate of Disaster Affairs of Turkey (AFAD),

German Research Center (GFZ), Italian Seismic Network (INGV), Seismological Network of Crete and Hellenic Unified Seismic Network (HUSN). For the inversion of the fault plane solutions we used the Generalized Cut and Paste code (gCAP) by (Zhu and Helmberger, 1996; Zhu and Ben-Zion, 2013). The method relies on filtering and shifting of 2 components of P_{nl} waveform windows and 3 components of the S and surface waveform windows separately and performing a grid search to find the earthquake mechanism and magnitude (Zhu and Ben-Zion, 2013). Green's functions were calculated using the velocity model from earthquake relocations (Table 3).

Source mechanisms of 29 earthquakes in the range of Mw 4 – Mw6.6, including the mainshock, were obtained and are tabulated in Table 4. We fixed the latitude and longitude of the earthquakes from our revised catalog. In addition to the best-fitting mechanisms we performed a centroid depth grid search in order to determine the centroid depth. The calculated centroid depths are consistent with the relocated catalog within an uncertainty of around ±1km (See Figure S7 caption for the details of the waveform inversion and Figure S7 for an example of waveform fits). For some events with M>4, it was not possible to model the earthquakes due to waveform complexity. Especially in the first few hours following the mainshock, the high seismic activity rate leads to interference of waves coming from different earthquakes which occur very close in time, making waveform modelling impossible.

In order to assess the uncertainties associated with the obtained source mechanisms, we performed a bootstrap analysis for 3 of the 29 earthquakes. We selected the events that have variance reduction around 50%, which is typical for this sequence. For each event, 1000 inversions are performed for the mechanism of the earthquakes by random resampling of stations. The results (Figure S8) show that the uncertainties in the strike, dip and rake values are below 10° and source mechanisms are well-resolved.

Finite-Fault Inversion

In order to find the slip distribution, we performed an inversion of two tracks of InSAR data as well as the GPS displacements using the finite-fault inversion of Ji *et al.* (2002), which finds a best-fitting

solution for the slip on a planar fault by minimizing the error using a simulated annealing algorithm. The error function consists of L_2-norm misfit to the geodetic data weighted based on their 1-σ uncertainties and the Laplacian smoothness constraint on the slip distribution. Since we do not have independent error estimates for the InSAR data, we assumed a 1-σ uniform uncertainty of 2.0 cm for all resampled InSAR measurements. This specific value was partly chosen in order to keep the weight on the inversion roughly the same for the GPS data and each InSAR track. For the InSAR data a static offset was added to the inversion parameters in order to account for the unknown zero level in each interferogram. For all the models, the Green's functions were calculated using the 1-D layered model in Table 3.

For the grid-search of best-fitting north and south-dipping fault planes, we used 13×13 sub-faults with sizes of 2.5 km × 1.7 km along strike and dip, respectively. After finding the location of the best fitting fault planes using the grid search, a wider fault plane was built with 27 and 16 sub-faults with size of 2 km × 1.35 km along strike and dip, respectively to find the final best-fitting solutions for both dip directions.

Results

Aftershock Locations and Mechanisms

Figure 2 shows the epicenter distribution of relocated aftershocks during the first 18 post-earthquake days, and the focal mechanisms of aftershocks obtained from regional waveforms (catalog available in the supplementary file). Most aftershocks occurred near the lateral terminations of the 2017 rupture. Figure S5 shows the time evolution of seismicity during the first 20 days of aftershocks. The early aftershocks surround the highest slipping region. In the following day the aftershock activity propagates in every direction and significant activity can be observed both toward the east and west. The cumulative activity shows that the 2017 earthquake triggered seismicity on fault systems as far as 40 km north of the coseismic fault (Figure 2, Figure S5).

Most aftershock source mechanisms are consistent with N-S extension, similar to the mainshock, especially those very close to the mainshock slip zone (Figure 2, Table S3), supporting models using planar fault geometries (e.g.,Karasözen *et al.*, 2018). However, there are some oblique mechanisms with small strike slip components, and some earthquakes with different orientations, including near the northwestern end of the rupture area where we find several NE-SW striking normal fault mechanisms. This change in orientation possibly marks the western end of the fault that ruptured during the 2017 event, consistent with fault maps that show a more NE-SW fault further west (Figure 2).

Grid Search for the Best-Fitting Fault Plane Location

As a first step of identifying the geometry of the earthquake fault, we performed a grid search to find the best-fitting fault plane location using both north and the south-dipping planes. For the strike and dip, we chose the Global CMT solution (Table 1). However, we also repeated the test using the USGS solution to show that our result is not dependent on small differences in strike and dip values. For each grid search point, we build a finite-fault and invert for the slip distribution using the geodetic data.

The model misfit is quantified by the sum of reduced chi-squared (χ^2_{ν}) error of GPS data and two tracks of InSAR data:

$$\chi^2_{\nu} = \frac{1}{N_{GPS}} \sum_{i=1}^{N_{GPS}} \left(\frac{d_i - m_i}{\sigma_i} \right)^2 + \frac{1}{N_{InSAR1}} \sum_{i=1}^{N_{InSAR1}} \left(\frac{d_i - m_i}{\sigma_i} \right)^2 + \frac{1}{N_{InSAR2}} \sum_{i=1}^{N_{InSAR2}} \left(\frac{d_i - m_i}{\sigma_i} \right)^2 \quad (1)$$

where d_i and m_i are the i^{th} data and model predictions, respectively. σ_i is the standard deviation of the i^{th} data point and N represents the number of data points for each three datasets.

Figure 3 shows the grid search for the best fitting location for the fault plane for the north and south-dipping planes, where every finite-fault model is represented by a grid point in the middle point the

fault plane at a depth of 6 km, and color represents the error of the finite-fault inversion as in equation (1). The grid search results show that while both fault planes can account for the geodetic data, the best-fitting north-dipping fault plane fits the geodetic observations (minimum $\chi^2_{\nu} = 1.82$) better than the south-dipping fault plane (minimum $\chi^2_{\nu} = 3.29$). In addition, there is a wider range of locations that fit the data for the north-dipping plane compared to the south-dipping plane (Figure 3).

In this study, we did not systematically change the strike and dip while performing the grid-search for finding the best-fitting fault plane location. Instead we relied on point-source mechanisms to fix the strike and dip of the fault plane. However, as mentioned above, we did try the same test using both fault planes based on USGS focal mechanism solution's strike and dip values (Table 1). The results of this test are very similar to those obtained from GCMT-based fault planes (Figure S9). This result shows that systematic preference of the north-dipping plane is not dependent on the variability of the fault plane strike and dip angles.

Best-Fitting North-Dipping and South-Dipping Slip Distributions from Finite Fault Models

In order to get the final, best-fitting north and south-dipping fault plane solutions, we performed the inversions for both fault planes with wider fault areas with finer sub-faults using their best –fit location obtained during the grid-search process. The geodetic misfit for the north-dipping plane (GPS $\chi^2_{\nu} = 0.66$, InSAR χ^2_{ν}=0.31, 0.44) is still significantly lower than the misfits for the south-dipping fault plane (GPS χ^2_{ν}=1.61, InSAR χ^2_{ν}=0.97, 0.52), clearly favoring a north-dipping plane.

Figure 4 shows the slip distribution and the fits to the GPS data for slip models for both dip directions. The slip distributions for both fault geometries show mostly a rupture toward the east. However, the slip model using the south-dipping fault plane indicates a longer rupture (~40 km) compared to the north-dipping plane solution (25 km) and it is less spread out at depth.

Comparison of the model fits to the coseismic GPS displacements shows that the vertical GPS in particular is better fit by the north-dipping model (Figure 4, inset). The south-dipping slip model overestimates the vertical displacements of the stations to the north of the fault plane while the horizontal vectors are slightly underestimated. The fits to the InSAR data show that the main difference is the estimation of subsidence on the southeast tip of Karaada (Figure 5). Specifically, vertical GPS displacements on the Bodrum coast, and the InSAR fringes on the island of Karaada, put tight constraint on the possible solution.

Figure 6 shows the profiles of aftershocks and their geometric relation to the two possible fault plane geometries. On the western profiles the north-dipping fault plane fits the depth distribution of seismicity better that the south-dipping plane. However, overall the distribution of hypocenters delineates no clear fault plane. Rather, the aftershocks occur throughout a broad (~100 km) region around the coseismic fault, consistent with the mainshock having triggered activity across a complex set of regional faults. As such, the distribution of aftershocks provides few constraints on the dip of the coseismic fault.

On the other hand, the location of the hypocenter is quite consistent with a north-dipping fault (Figure 6). The perpendicular distance of the hypocenter from the north-dipping fault plane is only 1 km. For the south-dipping plane, the distance of the hypocenter to the fault plane is 5 km, which is on the higher end of our estimation of location errors.

Coulomb Stress Changes due to Coseismic Slip and Early Aftershock Distribution

Although slip models with north and south-dipping fault planes generate similar displacements at geodetic data sites, the variations in slip distributions (Figure 4) generate different Coulomb stress perturbations at depth. Since the early aftershocks are expected to preferentially cluster in volumes of positive stress changes, the relationship between aftershock locations and stress changes can be used to identify a preferred coseismic model.

Towards this end, we calculated the Coulomb stress change on normal faults with the same mechanism as the mainshock, which is the dominant mechanism (Figure 2). Figure 7 shows depth slices of Coulomb stress change for the north and south-dipping faults along with the seismicity in that depth ±1 km during the first 5 days of aftershocks. The result shows that in the depth range of significant slip (4-10 km) the north-dipping model is more consistent with the seismicity. Especially at the depth slices of 8 and 10 km, the south-dipping model shows significant seismicity at zones of Coulomb stress decrease.

Discussion

Dip Direction and Slip Distribution of the 2017 Bodrum-Kos Earthquake

As described in the Introduction, the fault geometry of the 2017 Bodrum-Kos earthquake has been a subject of controversy since it occurred. Initial studies of the earthquake (Saltogianni *et al.*, 2017; Tiryakioğlu *et al.*, 2017) used a south-dipping fault model in order to model the co-seismic horizontal displacements.. Subsequent studies using horizontal GPS and the InSAR data, along with the mainshock and aftershock relocations, argued that the rupture occurred on a north-dipping fault (Karasözen *et al.*, 2018; Ganas *et al.*, 2019). Ganas *et al.*, 2019 systematically searched for the best-fitting south-dipping plane dimensions with constant slip and showed that the InSAR data is better explained by a north-dipping model.

In this study, by including vertical GPS displacements, additional campaign sites to the geodetic datasets, two additional tracks of InSAR data, and by systematically searching for the best-fitting fault plane using a grid search of finite-fault solutions, we obtained the best-fitting finite-fault solutions for both dip directions. Then we calculated the Coulomb stress change due to coseismic slip for both slip models and compared the stress perturbations to the early aftershock locations.

Our analysis shows that, a north-dipping coseismic fault plane provides a better fit to the geodetic data, is more consistent with the independently obtained hypocenter location, and accounts better

for the expected relationship between aftershock locations and Coulomb stress changes. Critically, the hypocenter location does not agree with the location of the south-dipping fault plane. When a fault plane that passes near the hypocenter is used, a south-dipping fault plane cannot fit the GPS observations. On the basis of these considerations, we conclude that a north-dipping fault ruptured during the 2017 earthquake, supporting the interpretations of Karasözen et al. (2018) and Ganas *et al.* (2019).

Our preferred geodetic slip distribution (Figure 4a) indicates that the earthquake ruptured a 20-25 km long patch toward east of the hypocenter between 2 and 10 km of depth range. The calculated peak slip is more than 2 m. The location of the hypocenter and the slip distribution shows that rupture is primarily to the east of the hypocenter. Our final slip distribution is similar to that reported by (Ganas *et al.*, 2017; Karasözen *et al.*, 2018).

Relationship to Regional Tectonics

The 2017 Bodrum-Kos Earthquake was one of many earthquakes that produced the present-day morphology of the Gulf of Gökova. The high rate of Pliocene extension directed towards the eastern Hellenic arc is consistent with the large number of M>5 historic earthquakes that have occurred in the Gulf, and dynamic models of Hellenic Trench rollback (e.g., Royden and Faccenna, 2018). Furthermore, the broad and dispersed distribution of aftershocks appears to indicate that the 2017 earthquake activated many other faults throughout the Gulf and surrounding areas (Figure 2).

Kurt *et al.* (1999) argue that in the eastern part of the Gulf, south-dipping faults are dominant, while in the west, a north-dipping fault system with a surface expression close to the southern coast of the Datça Peninsula is most prominent (Figure 2). The seismic sections by Kurt *et al.* (1999) show that at the western part of the Gulf, the sediments are thicker (~3.5 km) on the southern margin compared to the northern margin (< 1 km) which is possibly related to the activity of the north-dipping normal faults with surface expressions near the southern margin of the Gulf. To first order, our result

showing that the 2017 event occurred in the western Gulf on a north-dipping fault supports this view.

Karasözen *et al.* (2018) suggested that the fault that ruptured during the 2017 earthquake occurred on the western continuation of the North Datça Fault (Figure 2). Ganas *et al.* (2019) proposed that the fault that ruptured during the 2017 earthquake followed the Gökova Ridge, which is a 10 km E-W oriented topographic feature 5 km north of the South Datça fault. Whether the coseismic fault connects to the north-dipping South Datça Fault or directly projects to the Gökova Ridge remains to be further explored.

Conclusion

The 2017 Bodrum-Kos Earthquake ruptured the western segment of the Gulf of Gökova. Analyses of the mainshock source, GPS and InSAR observations of coseismic deformation, and consistency of the early aftershock distribution with the Coulomb stress change due to the coseismic slip distribution, all indicate that the 2017, M_w6.6, Bodrum-Kos Earthquake occurred on a ~40°, north-dipping, 20-25 km long, E-W striking, normal fault, with coseismic slip exceeding 2 m. Our preferred model locates the coseismic fault in the west-central Gulf where it accommodates N-S extension of the Gulf, and serves to separate Kos Island from the Bodrum Peninsula. N-S extension of SW Anatolia is related to the retreat of the easternmost Hellenic Trench that induces back arc, N-S extension and anticlockwise rotation of the Anatolia Extensional Province. The coseismic fault may be an eastward extension of the north-dipping Datça Fault.

Acknowledgements

The authors would like to thank the General Directory of Land Registry and Cadaster (TKGM), the General Directory of Mapping (HGM), the Association of Bodrum Geomatic Engineers and Greece NOANET for providing access to their GPS data. Also, the authors thank Mert Gurturk for his contribution at the GPS survey campaign. SAR data are copyrighted by the European Space Agency

and were distributed via the Alaska Satellite Facility. We would like to thank two anonymous reviewers for their detailed comments, which helped to improve the this paper significantly.

References

Aktug, B., J.-M. Nocquet, A. Cingoz, B. Parsons, Y. Erkan, P. England, O. Lenk, M. A. Gurdal, A. Kilicoglu, H. Akdeniz, and A. Tekgul 2009. Deformation of western Turkey from a combination of permanent and campaign GPS data: Limits to block-like behavior, *J of Geophys. Res.*, **114**(B10404), doi:10.1029/2008JB006000.

Akyol, N., L. Zhu, B. J. Mitchell, H. Sözbilir, and K. Kekovalı 2006. Crustal structure and local seismicity in western Anatolia, *Geophysical Journal International*, **166**(3), 1259-1269.

Bohnhoff, M., M. Rische, T. Meier, B. Endrun, D. Becker, H. P. Harjes, and G. Stavrakakis 2004. CYC-NET: a temporary seismic network on the Cyclades (Aegean Sea, Greece), *Seim.Res.Lett.*, **75**(3), 352-359.

Brüstle, A. (2012), Seismicity of the eastern Hellenic Subduction Zone, Ruhr-University Bochum, Bochum.

Chen, C. W., and H. A. Zebker 2002. Phase unwrapping for large SAR interferograms: statistical segmentation and generalized network models: , *IEEE Transactions on Geoscience and Remote Sensing*, **40**(8), 1709-1719.

Emre, O., T. Y. Duman, A. Dogan, S. Ozalp, F. Tokay, and I. Kuscu (2013), Active fault map of Turkey with explanatory text *Rep.*, General Directorate of Mineral Research and Exploration, Ankara, Turkey.

Farr, T. G., P. A. Rosen, E. Caro, R. Crippen, R. Duren, S. Hensley, M. Kobrick, M. Paller, E. Rodriguez, L. Roth, D. Seal, S. Shaffer, J. Shimada, J. Umland, M. Werner, M. Oskin, D. Burbank, and D. Alsdorf 2007. The Shuttle Radar Topography Mission, *Rev. Geophys.*, **45** RG2004.

Floyd, M. A., H. Billiris, D. Paradissis, G. Veis, A. Avallone, P. Briole, S. Mcclusky, J.-M. Nocquet, K. Palamartchouk, B. Parsons, and P. C. England 2010. A new velocity field for Greece: Implications for the kinematics and dynamics of the Aegean, *J of Geophys. Res.*, **115**(B110), https://doi.org/10.1029/2009JB007040.

Ganas, A., P. Elias, V. Kapetanidis, S. Valkaniotis, P. Briole, I. Kassaras, P. Argyrakis, A. Barberopoulou, and A. Moshou 2019. The July 20, 2017 M6.6 Kos Earthquake: Seismic and Geodetic Evidence for an Active North-Dipping Normal Fault at the Western End of the Gulf of Gökova (SE Aegean Sea), *Pure and Applied Geophysics*.

Ganas, A., P. Elias, V. S, P. Briole, V. Kapetanidis, I. Kassara, A. Barberopoulou, P. Argyrakis, Chouliaras, G, and A. Moshou (2017), Co-seismic deformation and preliminary fault model of the July 20, 2017 M6.6 Kos earthquake, Aegean Sea1*Rep.*

Görür, N., A. M. C. Şengör, M. Sakınç, O. Tüysüz, R. Akkök., E. Yiğitbaş, F. Oktay., A. Barka, N. Sarıca, B. Ecevitoğlu, E. Demirbağ, Ş. Ersoy, O. Algan, C. Güneysu, and A. Aykol 1995. Rift formation in the Gökova Region, Southwest Anatolia: Implication for the Opening of the Aegeran Sea. Geol. Mag. 132,637-650, *Geological Magazine*, **132**(06), 637-650.

Gurer, O. F., N. Sarica-Filoreau, M. Ozburan, E. Sangu, and B. Dogan 2009. Progressive development of the Büyük Menderes Graben based on new data, western Turkey, *Geological Magazine*, **146**(5), 652-673.

Gurolla, E. M., P. S. Agram, M. Lavalle, G. F. Sacco, and P. A. Rosen 2016. The InSAR Scientific Computing Environment (ISCE): An Earth science SAR processing framework, toolbox, and foundry, *AGU Fall Meeting*.

Heidarzadeh, M., O. Necmioglu, T. Ishibe, and A. C. Yalçıner 2017. Bodrum–Kos (Turkey–Greece) Mw 6.6 earthquake and tsunami of 20 July 2017: a test for the Mediterranean tsunami warning system, *Geoscience Letters*, **4**(31).

Herring, T. 1998. Documentation for GLOBK: Global Kalman filter for VLBI and GPS analysis program, *version 4.1, MIT*.

Herring, T. A., R. W. King, and M. A. Floyd 2015. Introduction to GAMIT/GLOBK Introduction to GAMIT/GLOBK Release 10.6, *Mass. Inst. of Technol., Cambridge*.

Ji, C., D. Wald, and D. V. Helmberger 2002. Source Description of the 1999 Hector Mine, California Earthquake, Part I: Wavelet Domain Inversion Theory and Resolution Analysis, *Bull. Seismol. Soc. Am.*, **92**(4), 1192-1207.

Karasözen, E., E. Nissen, P. Buyukakpinar, M. D. Cambaz, M. Kahraman, E. Kalkan Ertan, B. Abgarmi, E. Bergman, A. Ghods, and A. A. Ozacar 2018. The 2017 July 20 Mw 6.6 Bodrum–Kos earthquake illuminates active faulting in the Gulf of Gökova, SW Turkey, *Geophy. Jour. Int.*, **214**(1), 185–199.

Kissling, E., W. L. Ellsworth, D. Eberhart-Phillips, and U. Kradolfer 1994. Initial reference models in local earthquake tomography, *J of Geophys. Res.*, **99**(B10), 19635–19646.

Kurt, H., E. Demirbag, and I. Kuscu 1999. Investigation of the submarine active tectonism in the Gulf of Gökova, southwest Anatolia–southeast Aegean Sea, by multi-channel seismic reflection data, *Tectonophys.*, **305**477-496.

Lienert, B. R. E., E. Berg, and L. N. Frazer 1986. Hypocenter: An earthquake location method using centered, scaled, and adaptively least squares, *Bull. Seismol. Soc. Am.*, **76**771-783

McClusky, S., S. Balassanian, A. Barka, C. Demir, S. Ergintav, I. Georgiev, O. Gurkan, M. Hamburger, K. Hurst, H. Kahle, K. Kastens, G. Kekelidze, R. King, V. Kotzev, O. Lenk, S. Mahmoud, A. Mishin, M. Nadariya, A. Ouzounis, D. Paradissis, Y. Peter, M. Prilepin, R. Reilinger, I. Sanli, H. Seeger, A. Tealeb, M. Toksoz, and G. Veis 2000. Global Positioning System constraints on plate kinematics and dynamics in the eastern Mediterranean and Caucasus, *J. Geophys. Res.*, **105**(B3), 5695-5720.

Ocakoğlu, N., P. Nomikou, Y. İşçan, M. F. Loreto, and D. Lampridou 2018. Evidence of extensional and strike-slip deformation in the offshore Gökova-Kos area affected by the July 2017 Mw6.6 Bodrum-Kos earthquake, eastern Aegean Sea, *Geo-Marine Letters*, **38**211-225.

Ottemöller, L., P. Voss, and J. Havskov 2013. Seisan Earthquake Analysis Software For Windows, Solaris, Linux And Macosx

Reilinger, R., S. Mcclusky, P. Vernant, S. Lawrence, S. Ergintav, R. Cakmak, H. Ozener, F. Kadirov, I. Guliev, R. Stepanyan, M. Nadariya, G. Hahubia, S. Mahmoud, K. Sakr, A. Arrajehi, D. Paradissis, A. Al-Aydrus, M. Prilepin, T. Guseva, E. Evren, A. Dmitrotsa, S. V. Filikov, F. Gomez, R. Al-Ghazzi, and G. Karam 2006. GPS constraints on continental deformation in the Africa-Arabia-Eurasia continental collision zone and implications for the dynamics of plate interactions, *J of Geophys. Res.*, **111**(B05411), doi:10.1029/2005JB004051.

Rosen, P. A., E. M. Gurolla, G. Sacco, and H. Zebker (2011). InSAR Scientific Computing Environment (ISCE) – the home stretch, Abstract IN42A-02, paper presented at AGU Fall Meeting, San Francisco, CA.

Royden, L., and D. Papanikolaou 2011. Slab segmentation and late Cenozoic disruption of the Hellenic arc, *Geochem. Geophys. Geosys.*, **12**(3), doi:10.1029/2010GC003280.

Saltogianni, V., T. Taymaz, S. Yolsal-Cevikbilen, T. Eken, M. Gianniou, T. Ocalan, S. Pytharouli, and S. Stiros (2017), Fault-model of the 2017 Kos-Bodrum (east Aegean Sea) Mw 6.6 earthquake from inversion of seismological and GPS data – Preliminary Report*Rep.*, Istanbul Technical University.

Sengor, A. M. C., M. Satir, and R. Akkok 1984. Timing of tectonic events in the Menderes Massif, western Turkey: Implications for tectonic evolution and evidence for pan-African basement in Turkey, *Tectonics*, **3**(7), 693-707.

Simons, M., Y. Fialko, and L. Rivera 2002. Coseismic deformation from the 1999 M-w 7.1 Hector Mine, California, earthquake as inferred from InSAR and GPS observations, *Bulletin of the Seismological Society of America*, **92**(4), 1390-1402.

Tiryakioğlu, I., B. Aktuğ, C. Ö. Yiğit, H. H. Yavasoglu, H. Sözbilir, Ç. Özkaymak, F. Poyraz, E. Taneli, F. Bulut, A. Doğru, and H. Özener 2017. Slip distribution and source parameters of the 20 July 2017 Bodrum-Kos earthquake (Mw6.6) from GPS observations, *Geodin. Acta*, **30**(1), 1-14.

Vernant, P., R. Reilinger, and S. McClusky 2014. Geodetic evidence for low coupling on the Hellenic subduction plate interface, *Earth and Planetary Science Letters*, **385**122-129.

Yalçıner, A. C., A. Annunziato, G. A. Papadopoulos, G. G. Dogan, H. G. Guler, T. E. Cakir, C. Ozer Sozdinler, E. Ulutas, T. Arikawa, L. Suzen, U. Kanoglu, I. Guler, P. Probst, and C. Synolakis (2017), THE 20th July 2017 (22:31 UTC) Bodrum/Kos Earthquake and Tsunami; Post Tsunami Field Survey Report*Rep.*

Zhu, L., and D. V. Helmberger 1996. Advancement in Source Estimation Techniques Using Broadband Regional Seismograms, *Bull. Seism. Soc. Am.*, **86**(5), 1634-1641,.

Zhu, L., and Y. Ben-Zion 2013. Parametrization of General Seismic Potency and Moment Tensors for Source Inversion of Seismic Waveform Data, *Geophy. Jour. Int.*, **194**(2), 839-843.

TABLES

Table 1. Several point source mechanism solutions by global and local agencies.

	NP1 (stk°/dip°/rake°)	NP2(stk°/dip°/rake°)
Global CMT	278/36/-82	88/55/-96
AFAD	275/38/-80	82/53/-98
USGS	285/39/-73	84/53/-103
KOERI	286/53/-72	78/40/-112

AFAD: Disaster and Emergency Management Presidency (AFAD Turkey)
USGS: United States Geological Survey
KOERI: Bogazici University Kandilli Observatory And Earthquake Research Institute

Table 2. Details of Sentinel-1 InSAR data used in this study.

Track	Frame	Geom.	Subsw.	Date 1	Date 2	Baseline
131	114–119	asc.	1–2	2017/07/12	2017/07/24	-37 m
036	467–472	desc.	1–2	2017/07/12	2017/07/24	-5 m

Table 3. The velocity model for the region obtained from earthquake relocations.

Depth (km)	Vp (km/s)	Vs (km/s)
0.0	3.15	1.73
2.0	4.84	2.77
4.0	5.40	3.09
6.0	5.71	3.28
8.0	5.85	3.36
10.0	6.02	3.46
12.0	6.13	3.51
16.0	6.20	3.56
20.0	6.50	3.75
30.0	7.38	4.25
37.0	7.85	4.33

Table 4 Mechanisms of the mainshock and the aftershocks obtained in this study from regional seismic data.

Date	Time	Lat^{o}	Lon^{o}	Depth(km)	Mw	Stk^{o}	Dip^{o}	Rake^{o}
2017/07/20	22.31	36.959	27.43	12	6.48	94	48	-84
2017/07/21	0.15	36.958	27.4033	10	4.09	64	49	-63
2017/07/21	0.52	36.9403	27.4093	10	3.9	66	20	-87
2017/07/21	0.56	36.8796	27.6075	8.6	4.15	96	48	-65
2017/07/21	1.24	36.9625	27.4623	10.5	3.93	245	77	-74
2017/07/21	1.34	36.9055	27.5678	14.2	4.17	119	79	-42
2017/07/21	1.37	36.904	27.5743	9.5	4.34	123	84	-58
2017/07/21	1.49	36.986	27.414	14.1	4.16	247	70	-70
2017/07/21	2.11	36.8285	27.3521	0.5	4.4	291	44	-37
2017/07/21	3.58	36.8976	27.6031	13.9	4.22	85	66	-72
2017/07/21	5.12	36.9016	27.6203	1	4.13	91	67	-84
2017/07/21	5.51	36.922	27.3391	10.3	4.03	220	30	-60
2017/07/21	9.54	36.91	27.678	14.7	4.23	96	64	-74
2017/07/21	17.8	36.95	27.386	12.9	4.53	84	65	-68
2017/07/22	0.33	36.916	27.551	10.2	3.98	94	63	-70
2017/07/22	4.52	36.9	27.576	15.1	3.75	100	67	-62
2017/07/22	17.8	36.9143	27.3148	7.85	4.29	79	25	-90
2017/07/30	7.1	36.9956	27.5933	10.37	4.24	82	59	-81
2017/07/30	10.55	36.9913	27.6035	10.25	3.86	80	54	-73
2017/07/30	17.5	36.9601	27.6333	12.2	4.56	92	66	-71
2017/08/07	5.17	36.9951	27.6128	10.4	4.52	120	49	-50
2017/08/07	5.43	36.9616	27.6188	11.87	4.01	84	60	-77
2017/08/07	18.24	36.9905	27.6285	9.14	4.16	96	66	-71
2017/08/08	1.45	36.9738	27.6458	6.86	4.3	95	71	-83
2017/08/08	7.41	36.9576	27.6236	11.03	5.16	95	61	-72
2017/08/09	22.55	36.9783	27.6608	13.74	3.87	90	67	-66
2017/08/13	11.15	37.0813	27.6848	28	5	346	20	-21
2017/08/14	2.42	37.121	27.7088	7	4.69	111	71	-72
2017/08/18	14.9	36.9063	27.62	16.79	4.41	106	65	-79

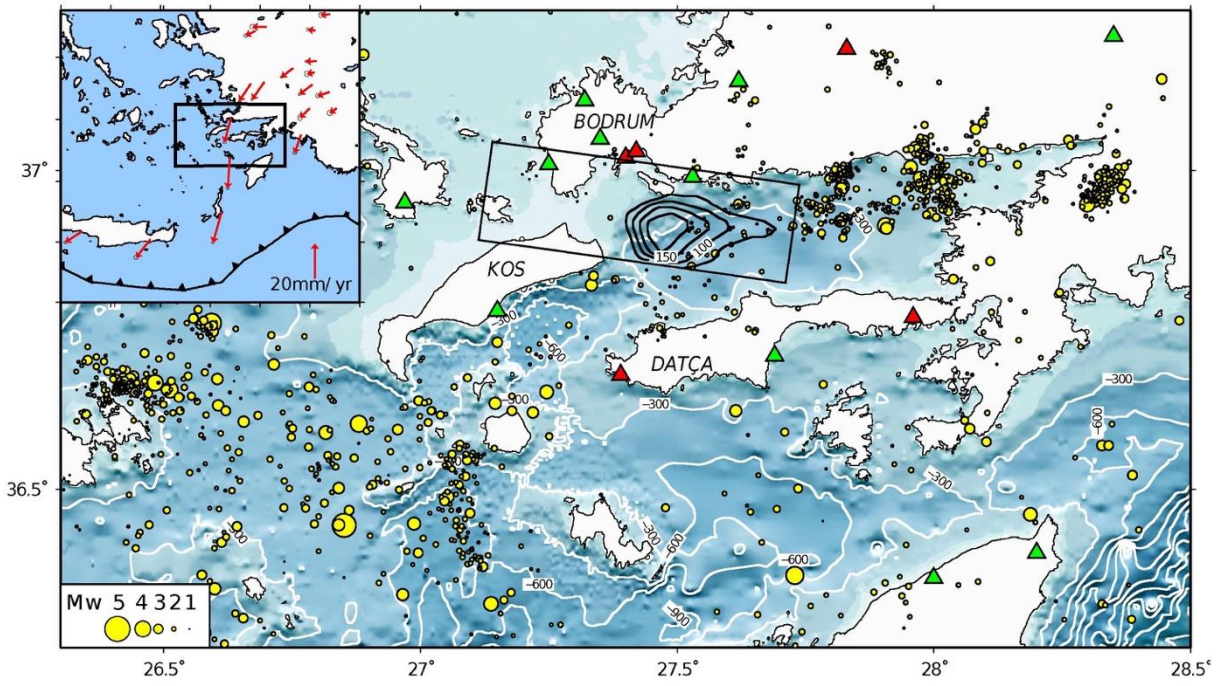

Figure 1. (Inset) Broader study area including the Hellenic Arc and the Aegean Sea region. The red vectors show selected annual GPS velocities with respect to Anatolia (Vernant *et al.*, 2014). The black box shows the area of the main figure. (Main Figure) The study region of the 2017 Bodrum-Kos earthquake. The black circles filled with yellow show the seismicity between 2002 and 2008 (Bohnhoff *et al.*, 2004; Brüstle, 2012) with magnitude scale on the bottom-left. The GPS stations used in this study are shown by green and red triangles for continuous and campaign sites, respectively. The black box represents the boundary of the best-fitting fault plane used for finite-fault modeling and the black enclosed curves show 50 cm slip contours for the best-fitting north-dipping slip model.

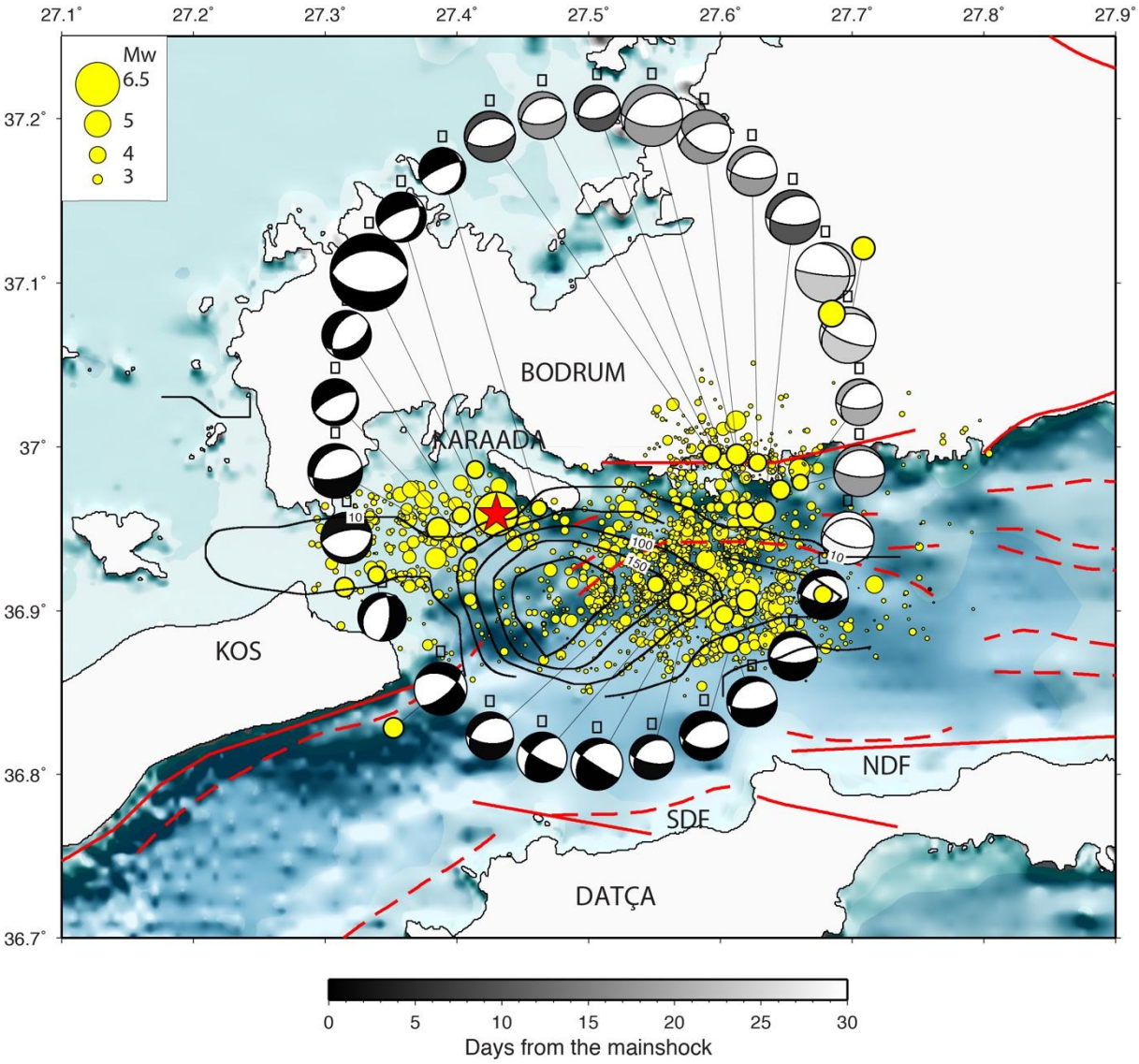

Figure 2. Map view of relocated mainshock, aftershock distribution and focal mechanisms. Focal mechanisms are colored in gray scale by their occurrence time and scaled in size by magnitude. Yellow circles show the epicenters of aftershock activity of the first 20 days in the vicinity of the main shock (M>1). The outermost black contour outlines the fault area that slips more than 10 cm. The other black enclosed curves show slip contours at every 50 cm for the final north-dipping slip model. Solid red lines indicate active faults in the region from active fault map of General Directorate of Mineral Research and Exploration (Emre *et al.*, 2013), while red dashed lines indicate faults from the study of Görür *et al.* (1995) and Kurt *et al.* (1999). Tick marks show the hanging wall of the identified normal faults from Kurt *et al.* (1999). SDF: South Datça Fault, NDF: North Datça Fault.

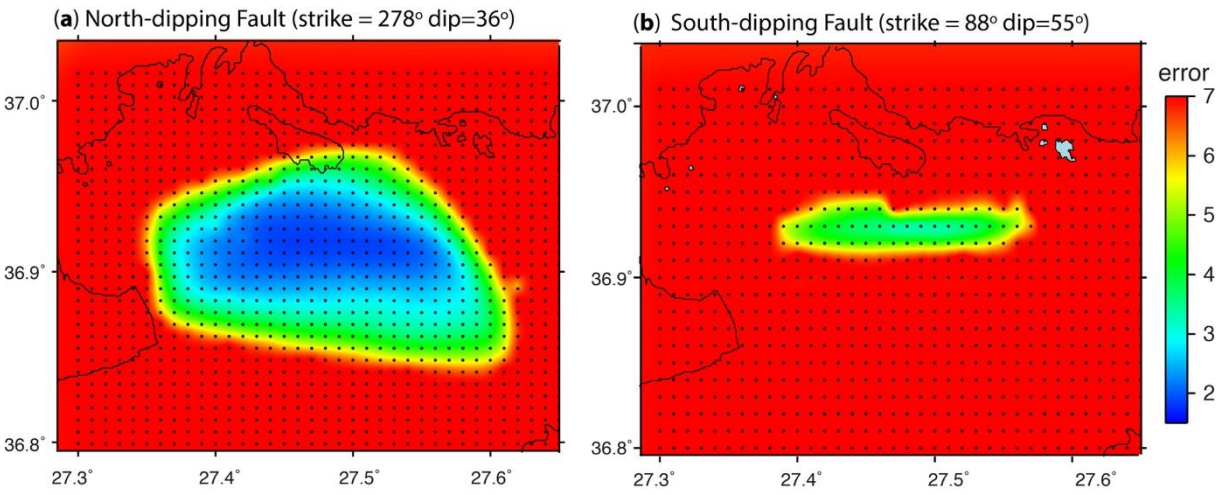

Figure 3. Results of the grid search for finding the location of the best-fitting fault plane for the **(a)** North-dipping fault planes (strike 278°, dip=36°), **(b)** South-dipping fault plane (strike=88°, dip=55°). Each black dot represents a finite fault model where the location of the dot represents the center point of the fault-plane along strike and 6 km depth .The χ^2 error values are saturated at 7.0 for both figures (see text for discussion).

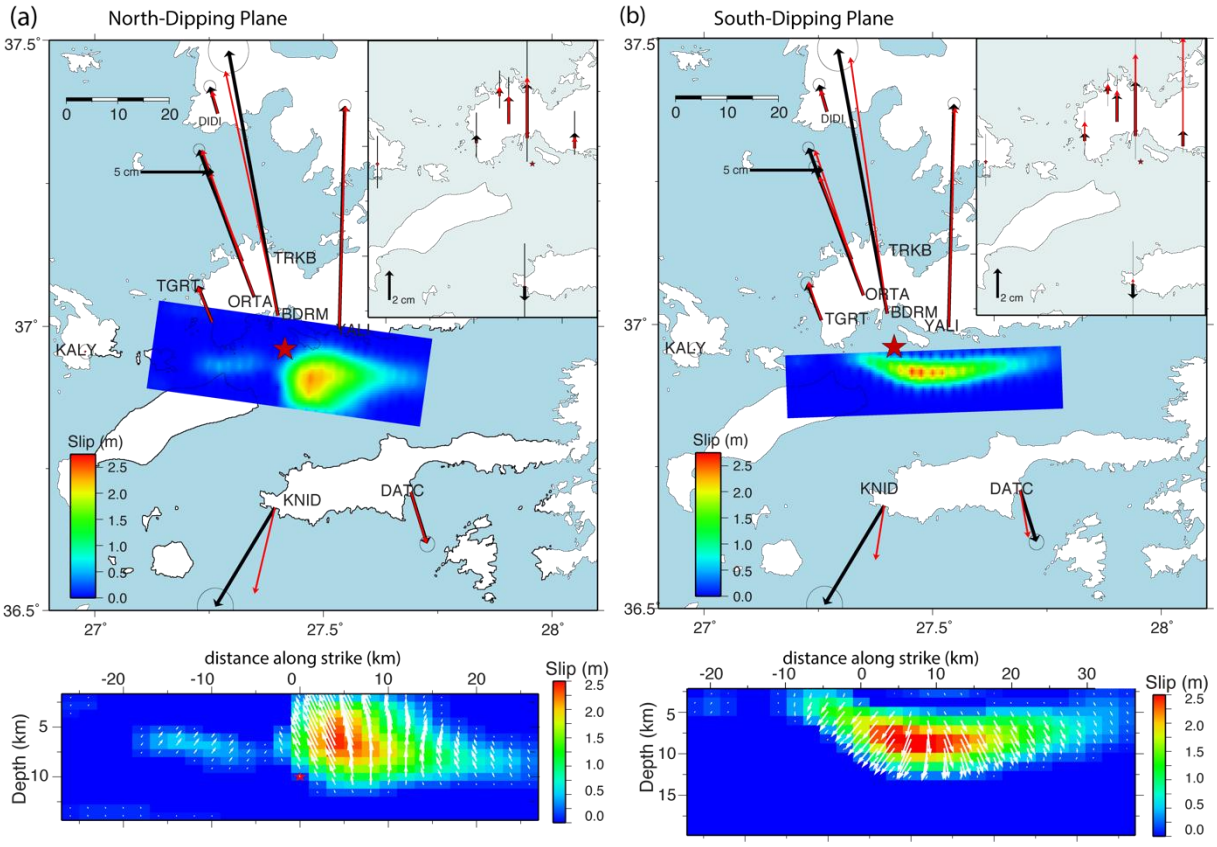

Figure 4. (a) (Top) Map view of slip distribution and horizontal GPS offsets (black arrows) and model predictions (red arrows) for the best fitting north-dipping fault. The inset shows the fits to the vertical GPS data. Coseismic uplift is shown by a vector pointing up and the vertical errors are shown by the black bars. Red star shows the epicenter location from this study. (Bottom) Fault plane view of the slip distribution for the north-dipping fault plane. The hypocenter obtained from relocation is also shown since it projects to the north-dipping plane. **(b)** Same as (a) for the south-dipping fault plane.

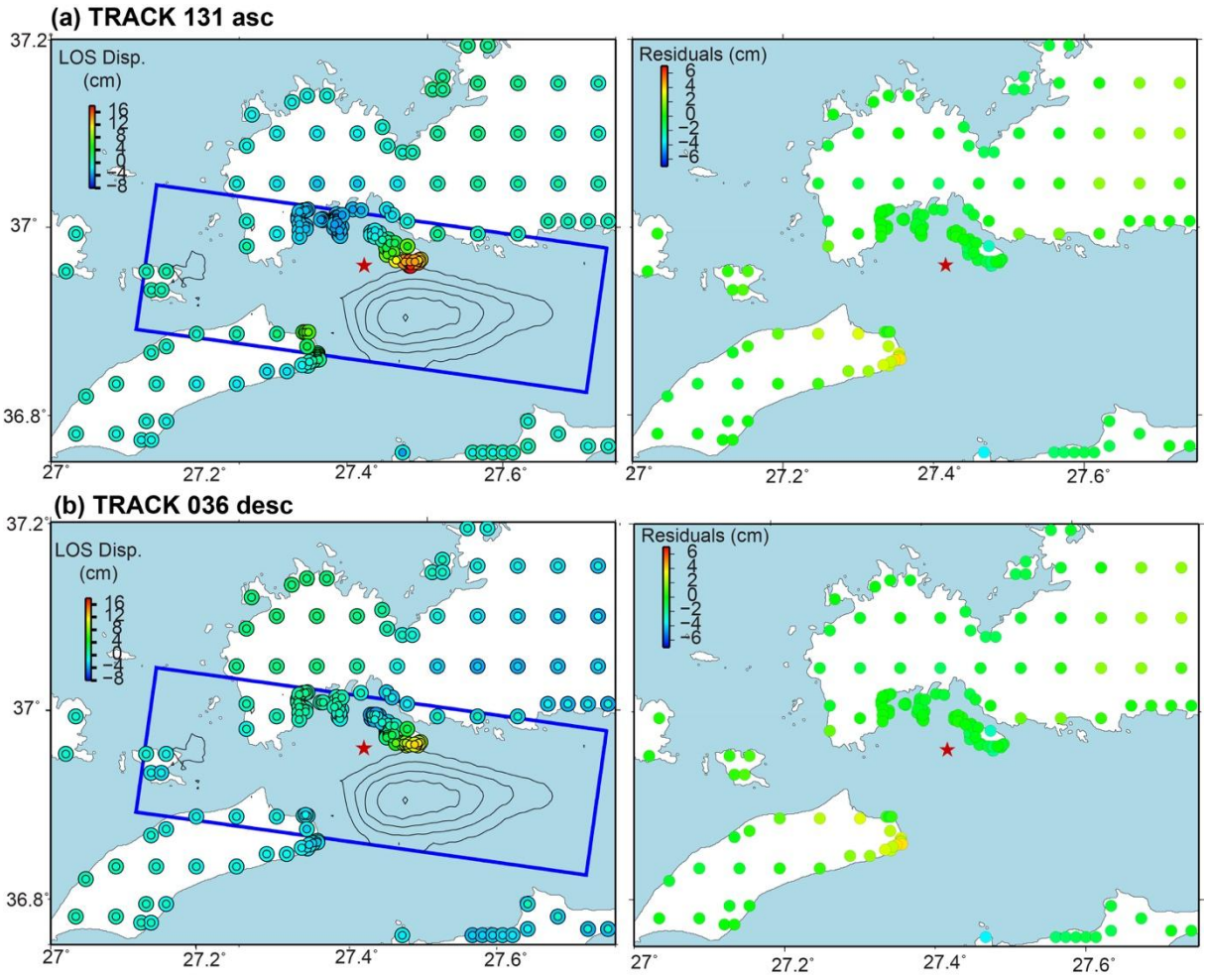

Figure 5. InSAR data for two tracks used in the modeling and the best-fitting north-dipping fault geometry. **(a)** (Left panel) InSAR data for ascending Track 131 along LOS direction (outer circles) and the model predictions (inner circles). The blue rectangle shows the edges of the fault plane and black enclosed curves show the 50 cm slip contours of the best-fitting north-dipping slip model. The red star shows the epicenter location of the of the mainshock. (Right Panel) The residuals for the model (data minus model prediction). The red star shows the epicenter location of the mainshock. **(b)** Same as (a) for the descending Track 036.

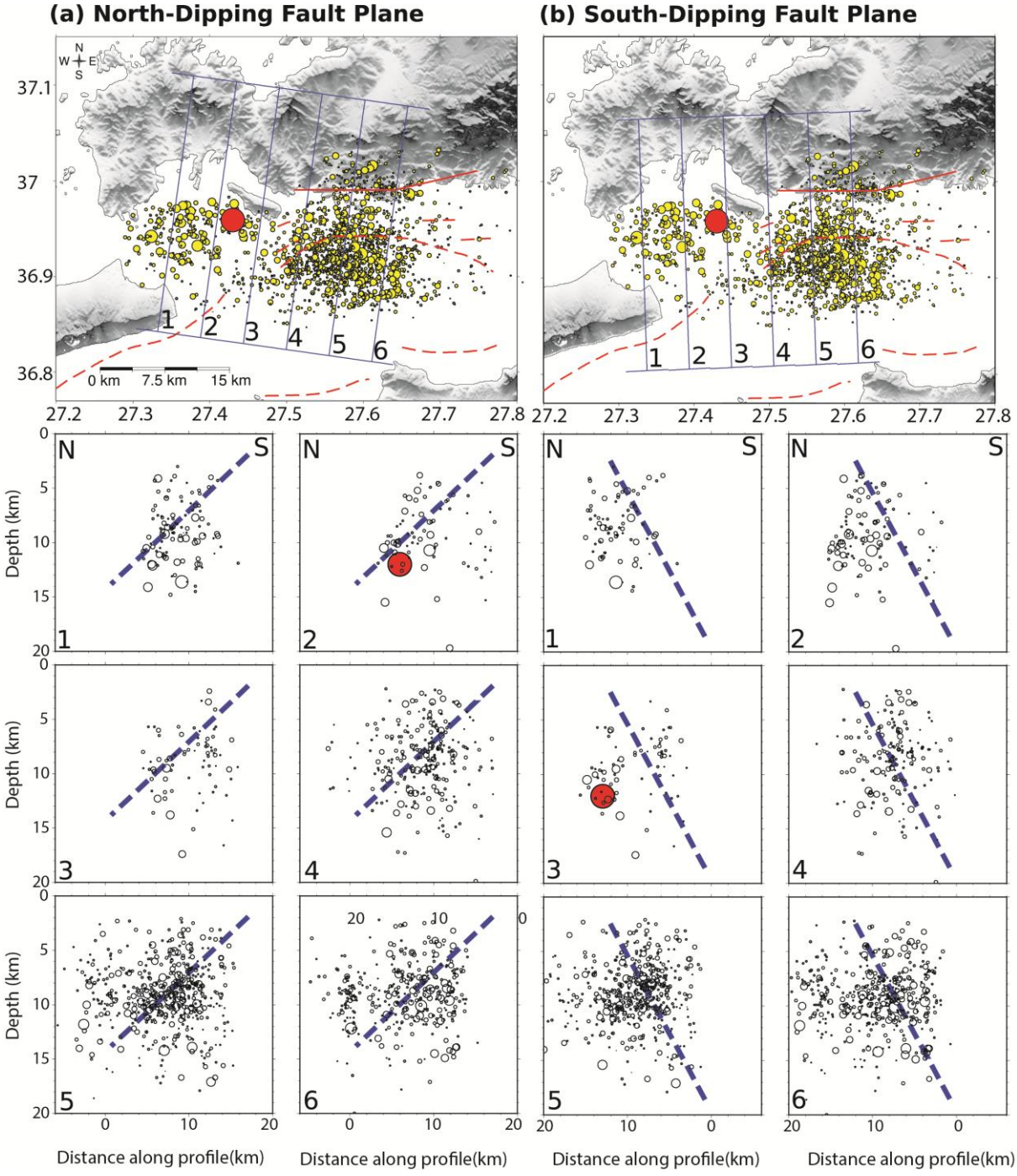

Figure 6. Seismicity distribution of the first 20 days with fault planes dipping to (a) north, and (b) south. Thick dashed lines show the fault plane. Red filled circle shows the location of the mainshock from this study. Each profile includes earthquakes within 2.5 km distance to the profile line in each direction. Red dashed lines show the fault lines from Emre *et al.* (2013) Görür *et al.* (1995) and Kurt *et al.* (1999).

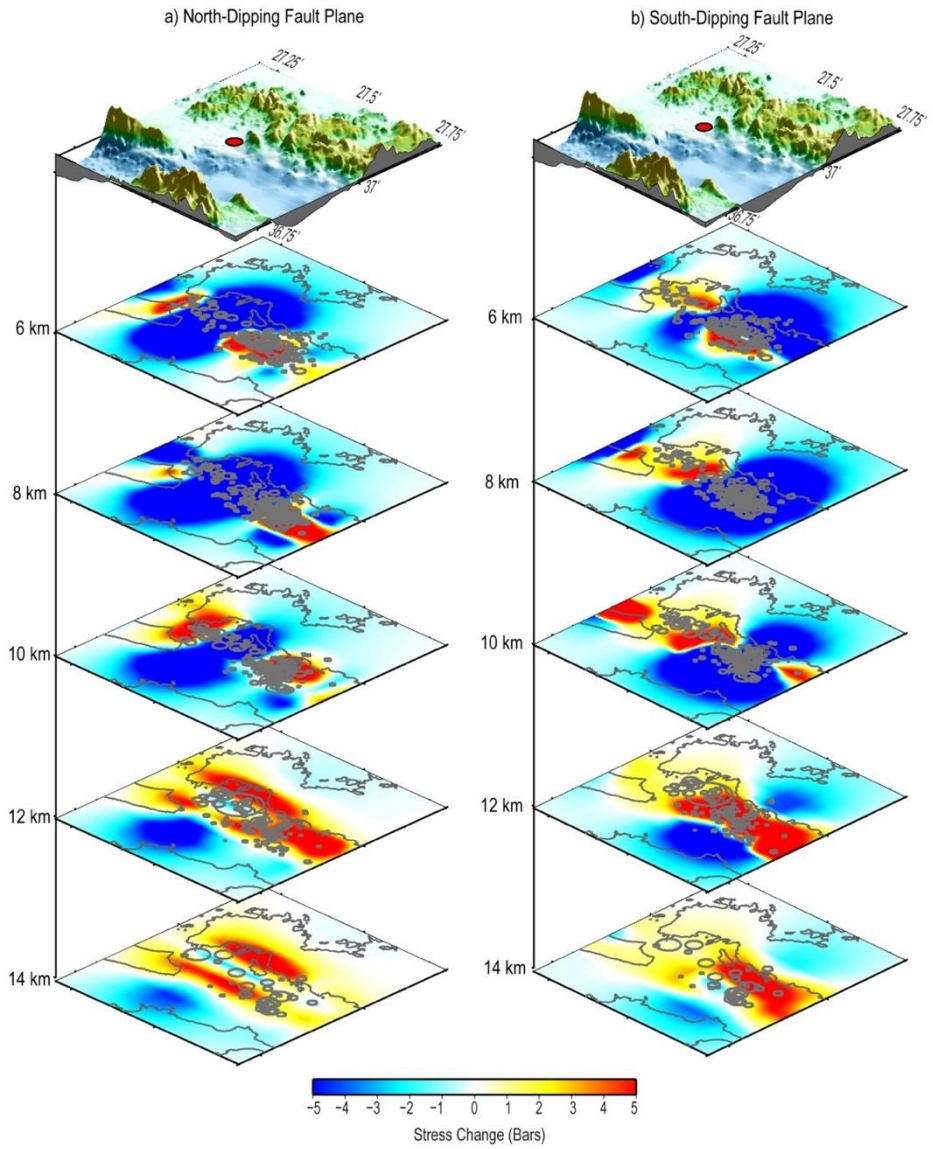

Figure 7. The Coulomb stress changes with the same mechanism as the mainshock for the (a) north-dipping (left panel) and (b) south-dipping (right panel) faults at depths between 4-14 km. The gray circles show the aftershocks (M≥1) during the first 5 days following the mainshock (between 2017/07/20 and 2017/07/25). Coulomb stress changes are calculated on faults having the same mechanism as the mainshock.